

Geophysical Research Letters®



RESEARCH LETTER

10.1029/2023GL105413

Key Points:

- High frequency optical satellites can detect the acceleration precursory to the Achoma landslide failure
- The acceleration follows a Voight law, classical of the tertiary creep of materials
- The time-series of ground displacement may be used to predict the time-of-failure for pixels of total displacement larger than 5 m

Supporting Information:

Supporting Information may be found in the online version of this article.

Correspondence to:

P. Lacroix,
pascal.lacroix@ird.fr

Citation:

Lacroix, P., Huanca, J., Albinez, L., & Taïpe, E. (2023). Precursory motion and time-of-failure prediction of the Achoma landslide, Peru, from high frequency PlanetScope satellites. *Geophysical Research Letters*, 50, e2023GL105413. <https://doi.org/10.1029/2023GL105413>

Received 21 AUG 2023

Accepted 17 SEP 2023

Corrected 16 OCT 2023

This article was corrected on 16 OCT 2023. See the end of the full text for details.


Author Contributions:

Conceptualization: P. Lacroix
Data curation: P. Lacroix, J. Huanca
Formal analysis: P. Lacroix, J. Huanca
Funding acquisition: P. Lacroix
Investigation: P. Lacroix
Methodology: P. Lacroix
Project Administration: E. Taïpe
Resources: P. Lacroix, J. Huanca, L. Albinez
Supervision: P. Lacroix, L. Albinez, E. Taïpe

© 2023. The Authors.

This is an open access article under the terms of the [Creative Commons Attribution License](https://creativecommons.org/licenses/by/4.0/), which permits use, distribution and reproduction in any medium, provided the original work is properly cited.

Precursory Motion and Time-Of-Failure Prediction of the Achoma Landslide, Peru, From High Frequency PlanetScope Satellites

P. Lacroix¹ , J. Huanca², L. Albinez², and E. Taïpe²

¹ISTERRE, University Grenoble Alpes, University Savoie Mont Blanc, CNRS, IRD, UGE, ISTERre, Grenoble, France,

²INGEMMET, Lima, San Borja, Perú

Abstract Landslide time-of-failure prediction is crucial in natural hazards, often requiring precise measurements from in situ instruments. This instrumentation is not always possible, and remote-sensing techniques have been questioned for detecting precursors and predicting landslides. Here, based on high frequency acquisitions of the PlanetScope satellite constellation, we study the kinematics of a large landslide located in Peru that failed in June 2020. We show that the landslide underwent a progressive acceleration in the 3 months before its failure, reaching at most 8 m of total displacement. The high frequency of satellite revisit allows us to apply the popular Fukuzono method for landslide time-of-failure prediction, with sufficient confidence for faster moving areas of the landslide. These results open new opportunities for landslide precursors detection from space, but also show the probable seldom applicability of the optical satellites for landslide time-of-failure prediction.

Plain Language Summary Many catastrophic landslides are preceded by specific movements, for example, a constant increase in velocity over time. These accelerations form the basis for predicting the landslide time-of-failure. The measurement of these movements is usually based on instruments installed on the landslide itself. However, this instrumentation is not always possible and, in recent years, the acquisition of satellite images at increasingly higher frequencies (e.g., PlanetScope satellites with a revisit frequency of less than 1 day) has raised interest in landslide monitoring and prediction. In order to assess the capability of PlanetScope satellites for this prediction, we analyze here the pre-failure movements of a large landslide in southern Peru, which collapsed in June 2020 and dammed a river. We show that the landslide underwent a progressive acceleration in the 3 months prior to its failure, reaching a total displacement of 8 m. Based on the displacement time-series of the fastest areas of the landslide, we predict the landslide time-of-failure 3 weeks in advance. Despite these encouraging results for landslide precursor detection from space, this study also shows the seldom use of optical satellites for landslide time-of-failure prediction.

1. Introduction

The time-of-failure prediction of landslides is a major operational goal of research on landslides, usually based on the monitoring of different physical parameters of the landslide, for example, displacement (Fukuzono, 1985; Mufundirwa et al., 2010; Saito, 1969) or seismic activity (Poli, 2017; Schöpa et al., 2018). This prediction has been applied with different degrees of success to numerous case-studies, where precursory motions before landslide failure have been observed (Federico et al., 2012; Intrieri et al., 2019).

Landslide motions prior to a rupture can exist for different types of failure mechanisms. For landslide motions controlled by the water-pore pressure at the sliding surface, transition from slow to rapid motions can be caused by a pore-water pressure exceeding a certain threshold (Iverson & Major, 1987). In this case, slow motions with seasonal patterns are usually observed that allow a detection of the unstable areas, but no general clear precursory signs before failure exist that can be used to predict failure occurrence. For some case-studies, authors have shown that analyzing the specific kinematic behavior of one slow-moving landslide compared to the surrounding ones in the same lithology can help to identify a landslide in transition toward failure (Handwerker et al., 2019).

Some other landslides develop progressively thanks to the progressive maturation of the sliding surface (Bruckl & Parotidis, 2005; Eberhardt et al., 2004; Forlati et al., 2001; Muller & Martel, 2000), a mechanism that is typical of the tertiary creep of many materials (Voight, 1989), and classically explained by subcritical crack

Validation: P. Lacroix, J. Huanca, L. Albinez
Writing – original draft: P. Lacroix
Writing – review & editing: P. Lacroix, J. Huanca

growth processes (Bruckl & Parotidis, 2001). This mechanism is characterized by a last kinematic phase with accelerating displacement until the rupture (Bhandari, 1988; Zvelebill & Moser, 2001). This accelerating pattern is a real opportunity for landslide prediction, and different methods have emerged to predict the time-of-failure of landslides based on this mathematical law. The most popular one is the Fukuzono method (Fukuzono, 1985) which relates the time-of-failure of the landslide to its inverse velocity thanks to a power-law coefficient α . For landslides, α is found to vary from 1.3 to 3.3 (Crosta & Agliardi, 2003; Federico et al., 2012; Intrieri et al., 2019). Assuming $\alpha = 2$ leads to a linear relation between inverse velocity and time, which makes the method easy to apply to real data.

The inverse velocity method is widely used, even on an operational basis, mostly in mines (Rose & Hungr, 2007), based on time-series of landslide displacement from in situ measurements, coming from terrestrial laser scanning, extensometers, ground-based SAR, or global navigation satellite systems (GNSS). These measurements have the advantage of a high frequency rate and low uncertainties, required to derive velocity time-series. They also have the drawbacks of being punctuated, and require instrument maintenance. Most of all, these measurements require the landslide to be detected and instrumented before its failure, which is rarely the case. Remote sensing of slopes is thus of real interest for landslide prediction (Casagli et al., 2023), either from terrestrial cameras that scan a certain limited area (typically at a slope scale) or from airborne or satellites. However, the noise of satellite remote sensing processing to derive ground surface displacement and their frequency of acquisition raise questions about the ability of satellites to detect these accelerations and predict their time-of-failure (Carlà et al., 2019; Intrieri et al., 2018; Lacroix et al., 2018; Moretto et al., 2017).

The development of time-series techniques and the increase of satellite revisit time has enabled the generation of high frequency time-series of landslide displacement (Intrieri et al., 2018; Lacroix et al., 2018). This spatially dense and increasingly temporally-resolved data set has enabled scientists to show the high variability of landslide kinematics at different time-scales, mostly focusing on non catastrophic landslides (Handwerker et al., 2013, 2015; Lacroix et al., 2019). However, at least 5 studies show the possibility for satellites to detect landslide pre-failure accelerations before their transition from slow to rapid motions (Carlà et al., 2019; Handwerker et al., 2019; Intrieri et al., 2018; Lacroix et al., 2018; Li et al., 2020) either using InSAR, or correlation of SAR or optical images.

Different limitations arise from the analysis of these different case-studies. First of all, the acceleration phase can produce very small displacements, hardly visible in the satellite image processing. For instance, on the Xianmo landslide the displacement observed by InSAR during the acceleration phase is only 4 cm (Intrieri et al., 2018). Then, the landslides can have quick accelerations relative to the sampling frequency. On the Xianmo landslide the acceleration is seen only over 6 Sentinel-1 acquisitions (Intrieri et al., 2018). On the Harmalière landslide, the acceleration, accommodating 4 m of displacement in 3 days, is seen only over 2 Sentinel-2 acquisitions (Lacroix et al., 2018). This low number of data points in the acceleration period prevents the prediction of the landslide time-of-failure. Very few case studies show substantial and long-lasting landslide accelerations seen with satellites. To our knowledge, this was observed only on the Baige landslide (Li et al., 2020), where the acceleration phase occurred over 1.5 years, with cumulative motions reaching 45 m. Usually, acceleration may occur over much shorter periods, with smaller magnitudes (Moretto et al., 2017). In this context, high frequency satellites like the PlanetScope cubesat constellation (Roy et al., 2021) offer a unique opportunity to increase the temporal sampling of these accelerations. Despite their sensitivity to cloud cover, one main advantage of optical image correlation compared to InSAR is its ability to resolve large motions over short period of times, and the possibility to obtain easily-interpretable 2D displacements. In this study we evaluate the potential of PlanetScope satellites to detect pre-failure accelerations and to predict landslide time-of-failure. For that purpose we back analyze a large landslide in Peru that failed catastrophically in June 2020.

2. Study Site

The Colca area, situated in South Peru (Figure 1), is a deep river incised valley inside lacustrine deposits from a paleo-lake of 30 km long. The terraces have allowed for villages and agriculture settlements for several millennia. The Colca river erodes the lacustrine deposits and trigger landslides that can then be remobilized by the seasonal rainfall infiltration (Zerathe et al., 2016) and M5+ earthquakes (Bontemps et al., 2020). Many rapid and slow-moving (m/yr) landslides were detected in the area, based on the comparison of DEMs (Zerathe et al., 2016) and the correlation of diachronic optical images (Bontemps et al., 2018; Lacroix et al., 2015; Pham et al., 2018).

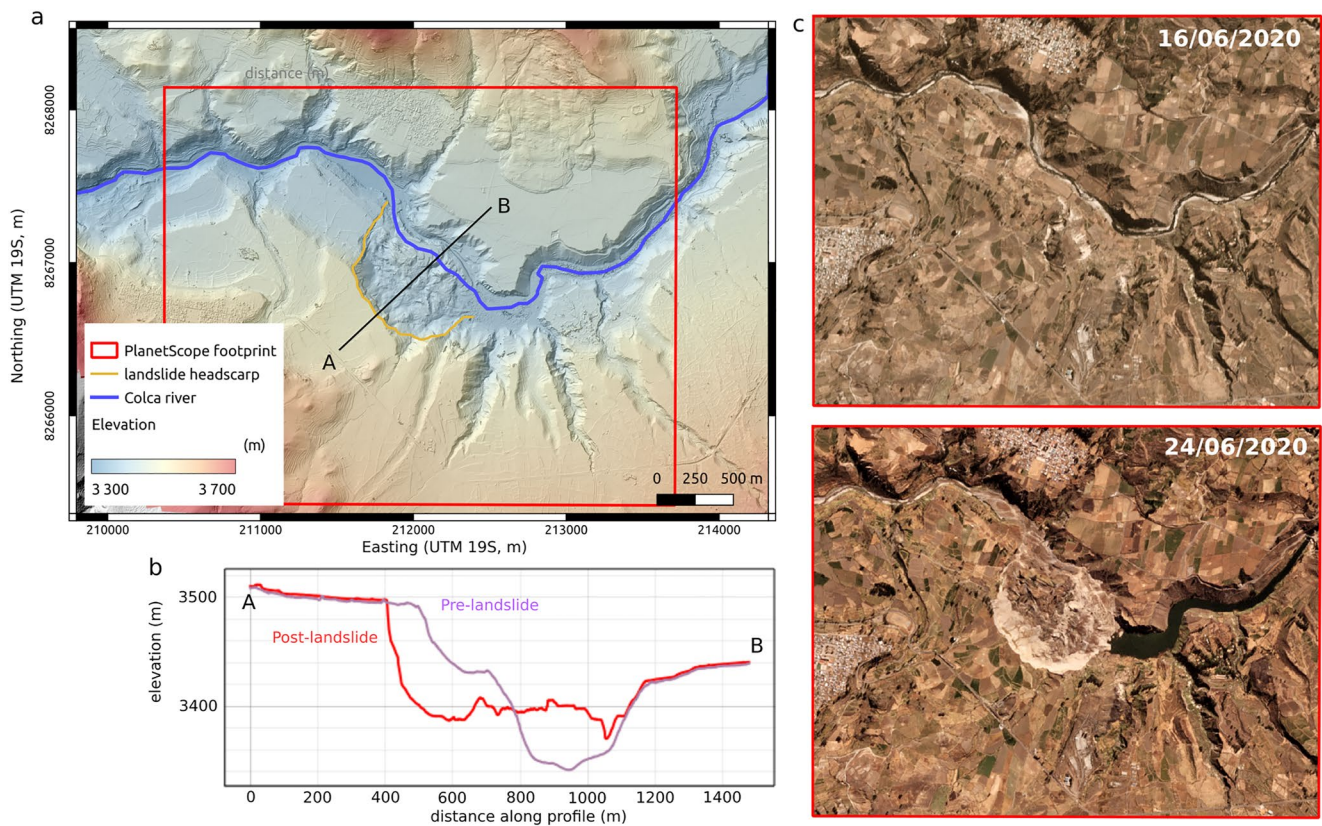


Figure 1. Digital elevation Model of the area (a). Topography along the profile A-B before/after the event (b) measured using Pléiades and drone acquisitions (see Figure S3 in Supporting Information S1). PlanetScope image before/after the landslide occurrence (c).

The large Achoma landslide (picture in Figure S1 in Supporting Information S1), which failed the 18th of June 2020, is connected to the river. The first signs of activity, mostly vertical cracks, were reported by local inhabitants in May 2020. The landslide failure occurred during the night, but several seismic sensors situated between 8 and 70 km away detected the signal generated by the Achoma landslide failure (Vela Valdez & Chacaltana, 2020), dating the landslide occurrence to the 18th of June 2020 at 6h42 UTC. The rainy season stopped mid April 2020, so this failure occurred during the dry season. The triggering factor of this landslide is still an open question.

Digital Elevation Models were obtained before (2017/5/13) and right after (2020/06/19) the landslide, thanks to the processing of Pléiades (Lacroix et al., 2015) and drone acquisitions (see Figure 1b and Supporting Information S1), allowing the quantification of its characteristic size. The landslide is 800 × 500 m in size and the landslide headscarp, nearly vertical, is more than 100 m high. The landslide affects a zone of agriculture, and dammed the river, creating a lake upstream (Figure 1d). The risk of flooding posed by this dam was quickly solved by engineers digging inside the landslide mass and creating a path for the river flow.

2.1. PlanetScope CubeSat Images

In order to study the pre-failure motion of the landslide, we realized a time-series of ground displacement using the high-frequency PlanetScope satellites. The complete PlanetScope constellation, composed of approximately 180 satellites is able to image the entire land surface of the Earth every day (Roy et al., 2021). Each PlanetScope satellite is a CubeSat 3U form factor. Three generations of PlanetScope satellites have been launched since July 2014, with increasing footprints and multispectral capabilities. The third generation provides images after March 2020, so the images processed here are coming mostly from the two first generations. These two generations have similar characteristics (https://assets.planet.com/docs/Planet_Combined_Imagery_Product_Specs_letter_screen.pdf), namely a four-band frame imager, with resolution between 3 and 4.1 m resampled to 3 m. The data are provided at different levels of processing on the webserver (<https://www.planet.com/explorer/>). After several

trials, we used the “PlanetScope Scene” product to avoid the mosaicking of different stripes of images acquired with different viewing angles on the same day. In this manner, we control the mosaicking of the images over the selected area and ease its correction.

We selected 79 images over an area of $3.3 \times 3 \text{ km}^2$ (Figure 1), with a frequency of 1 per month during the low velocity period of the landslide from November 2017 to December 2019 to estimate the seasonal errors due to shadowing effects (Lacroix et al., 2019) and then all available cloud-free images in the period of interest from January to June 17 2020 (Table S2 in Supporting Information S1), corresponding to the last acquisition day prior to the landslide rupture.

2.2. Displacement Time-Series

A time-series of horizontal ground displacement is calculated following the approach developed in Bontemps et al. (2018) and adapted for the PlanetScope images (Figure S4 in Supporting Information S1): (a) correlation of all the pairs of images using Mic-Mac (Rupnik et al., 2017), which is well suited to images of low radiometric contrasts or small objects (Lacroix et al., 2020), (b) masking the low correlation coefficient values ($CC < 0.7$), (c) mosaicking correction, similar to stripe corrections (Bontemps et al., 2018), that we obtained by subtracting the median value of the stacked profile in the along-stripe direction, taking into account only stable areas, (d) least square inversion of the redundant system per pixel, weighted by the time separation between pairs (Bontemps et al., 2018), (e) correction of illumination effects (Lacroix et al., 2019), based on the 2 years of data between November 2017 and December 2019.

This method, now implemented on operational platforms (e.g., GEP, Form@ter DSM-OPT) (Provost et al., 2022), has been validated for landslide studies of different areas using SPOT1-5 (Bontemps et al., 2018), Sentinel-2 (Lacroix et al., 2020; Provost et al., 2022), Landsat-5/7/8 (Lacroix et al., 2019, 2020) images. The uncertainties of the EW and NS displacement fields are estimated by the NMAD estimator (Höhle & Höhle, 2009) of the displacement field on the stable areas at each time-step (Figure S5 in Supporting Information S1).

2.3. Time-Of-Failure Prediction

The most popular method for landslide time-of-failure prediction, the inverse velocity method, is based on a Fukuzono model (Fukuzono, 1985). This latter provides an analytical solution for the landslide velocity v to the common Voight law (Voight, 1989), that links the acceleration a and the velocity of any material in its final stage of acceleration under conditions of approximately constant stress, through two constants A and α :

$$a(t).v(t)^{-\alpha} = A \quad (1)$$

$$v(t) = (A(\alpha - 1)(t_f - t))^{\frac{-1}{\alpha-1}} \quad (2)$$

With t_f the time-of-failure. In the case of $\alpha = 2$, $1/v$ becomes linear with t , and t_f is therefore obtained by extrapolating the linear relation between the inverse-velocity of the landslide and time up to the zero inverse-velocity. This method is therefore applied on landslide velocity time-series, not displacements. Due to large uncertainties in the ground displacement values from optical satellites (see Section 3.1), the simple time derivation of the ground displacement time-series leads to unreliable velocities. Previous authors dealing with such problems first filtered the displacement time-series before their derivation, using different types of median filters or moving averages (Bozzano et al., 2018; Carlà et al., 2017; Intrieri et al., 2018; Sharifi et al., 2022; Zhang et al., 2021). These filters rely on a sufficiently high rate of observations, which can be common with in-situ measurements but not with satellite remote sensing.

Here we adapted the strategy previously used by Azimi et al. (1988), which consists of evaluating the velocity of the landslide over segments of equal displacement, to reduce the effect of noise in the displacement data. This idea takes advantage of the monotonic direction of the landslide displacement with time to provide more robust time-series. We adapt this strategy to consider the displacements not directly on the raw values but rather on linear fits of the raw values with time (see Figure S6 in Supporting Information S1).

3. Results

3.1. Landslide Kinematics

The maps of cumulative displacements over the 2.5 years of measurements display a ground motion before the landslide rupture of between 3 and 8.1 m, located exactly on the mass that collapsed on the 18th of June 2020

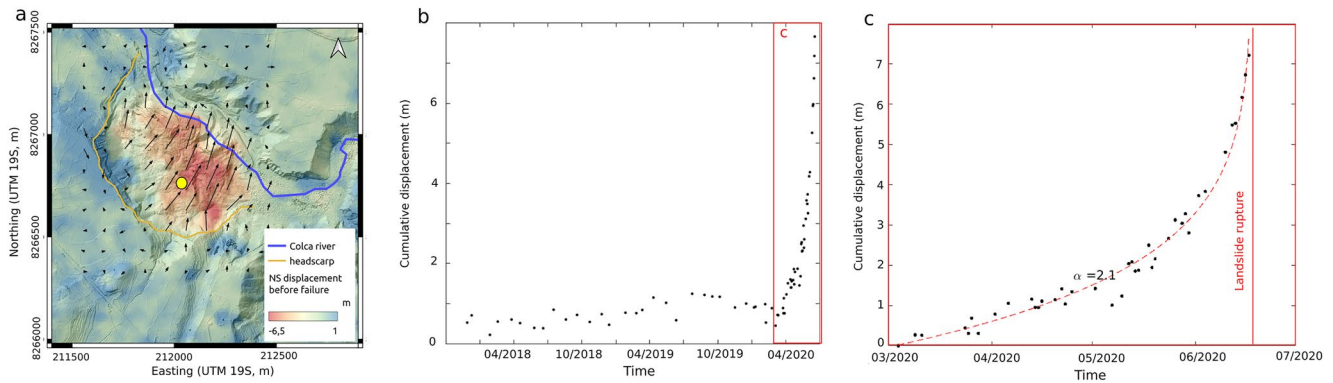


Figure 2. Results of the time-series processing on the Achoma landslide: (a) map of cumulative displacement over 2.5 years before the failure, (b) time-series of cumulative displacement on one specific point (shown with a yellow dot on the map of subplot (a)), (c) zoom over the last 3 months display in the progressive acceleration. The red dashed line represents the best fit of the Fukuzono model, fixing t_f to its real time.

(Figure 2). Stronger motions are encountered at the toe than at the headscarp location, suggesting either a fragmentation of the mass, or a rotational component of the landslide with a motion being mostly vertical at the headscarp and mostly horizontal at the toe. This last explanation is more plausible given the highly vertical headscarp of more than 100 m height observed after the landslide failure.

Around the landslide area, no clear signals of deformation are visible. The uncertainties (Figure S5 in Supporting Information S1), calculated on these stable areas, are between 0.2 and 0.9 m in EW and 0.2 and 1.2 m along the NS component, with a seasonal variation due to the seasonal variation of the shadows (Lacroix et al., 2019) in addition to a slight linear trend with time. Some dates clearly exceed this seasonal variation, so we remove these outliers (8 points out of 79 dates, see Figure S5 in Supporting Information S1). The behavior of all individual pixels on the landslide display a similar pattern with time, with a slow motion from November 2018 to March 2020, followed by a progressive acceleration over 3 months until the rupture on the 18th of June 2020 (Figure 2).

3.2. Landslide Acceleration Modeling

To better understand the physics behind the general pattern of acceleration, we first approximated the mathematical law of this acceleration using the classical Fukuzono model (see Equation 2). We fixed the time of failure t_f , known from seismic sensors (Vela Valdez & Chacaltana, 2020), and inverted the other parameters of the model by minimizing the norm of the difference between the displacement time-series observed and the modeled one using a grid search over the parameters A and α . The Fukuzono model gives an analytical solution for the velocity, so that we integrate numerically the velocity to have a value for the modeled displacement. This inversion process leads to $\alpha = 2.14 \pm 0.12$ for the pixels with sufficiently large acceleration to be well resolved (Figures S7 and S8 in Supporting Information S1). We also find that α and A are not fully independent (see Figure S9 in Supporting Information S1).

3.3. Landslide Prediction

We now test the ability of this data set to predict the time-of-failure, by fixing $\alpha = 2$ (despite we know that it is not exactly true), in order to use the classical inverse velocity model, and therefore invert t_f . The time-series of displacement are highly noisy, with uncertainties of about 0.8 m for maximum pre-failure displacements of 8.1 m. Therefore, the question can be raised about their utility for landslide prediction.

We extract the velocity time-series from the displacement time-series by applying the algorithm presented in Section 2.3 to the pixels situated on the landslide. The time-series of velocity display an acceleration starting from the end of 2019 with values exceeding 1 cm/day around 1 March 2020 (Figure S6 in Supporting Information S1). The inverse-velocity method applied to this data set is not strictly following the $\alpha = 2$ regime, so that the linear fit over the last dates is contaminated by the previous measurements (Figure 3; Figure S10 in Supporting Information S1). To partly overcome this limitation, the linear regression of the inverse velocity with time is weighted by the inverse of the uncertainties of each velocity estimation, which are lower when the velocities are higher,

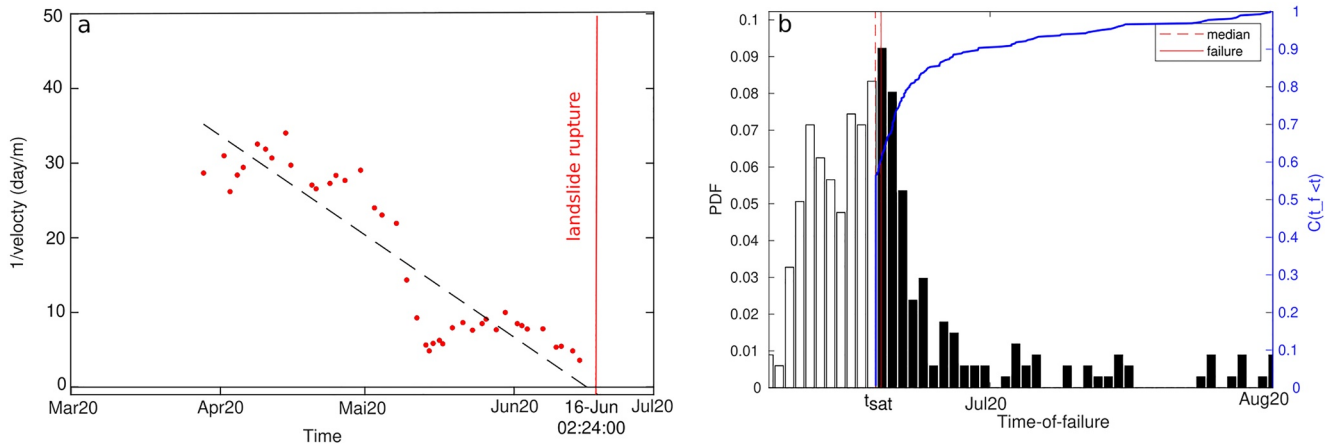


Figure 3. (a) Inverse velocity obtained for one specific point and linear fit (dashed black) leading to a prediction for t_f of 16-June-2020 at 2:24. (b) PDF (white/black bars) and CDF (blue curve) of time-of-failure for all the points of the landslide using the whole time-series up to the last acquisition of 17th of June. The white bars in the PDF represent the t_f prediction before the last satellite acquisition.

that is close to the rupture. Using this method, a time-of-failure is obtained for every pixel of the landslide. Given the constraint that the time-of-failure occurs after the last satellite acquisition, the empirical probability density function (pdf) of the time-of-failure is positively skewed (Figure 3 and Figure S11 in Supporting Information S1).

We choose to characterize this pdf with two values: the median of the pdf (M_{pdf}), and the probability (P_3) to have a failure within 3 days after the last satellite acquisition (t_{sat}). The cumulative density function $C(t_f < t)$ is first calculated:

$$C(t_f < t) = \sum_{t_{sat}}^t pdf \quad (3)$$

P_3 is then obtained by calculating $C(t_f < t)$ for $t = t_{sat} + 3$ days. These 3 days are chosen as it may be an acceptable time required to process the last acquired image, analyze the results, and eventually deliver an alert to the populations.

At the time of the last satellite acquisition ($t_{sat} = 17$ th June), the M_{pdf} is found to be t_{sat} (Figure 3b), due certainly to a value of α greater than 2. The probability P_3 to have a landslide failure within 3 days is found to be 0.72.

We can wonder how long in advance could we have predicted the time-of-failure of this event. For that purpose, we removed iteratively the last satellite acquisition and recalculated the time-series of velocities and the resulting t_f prediction using the inverse velocity method. This process gives us a landslide time-of-failure estimate as a function of the last satellite acquisition t_{sat} of the time-series (Figure S11 in Supporting Information S1). For each one of these time-series we also calculate M_{pdf} and P_3 for groups of pixels that have different motion magnitudes (4–5 m, 5–6 m, 6–7 m, greater than 7 m) (Figure 4). The results show that for pixels of large motions (displacement greater than 7 m, 28% of the total pixels of the landslide), M_{pdf} is fairly stable over the last 3 weeks before the failure, and estimates a time-of-failure within less than 8 days of the real rupture. For pixels with motions between 5 and 7 m, M_{pdf} follows the same pattern but with less precision. For pixels with total motions less than 5 m, M_{pdf} is always increasing with time and never converges.

The probability P_3 is always increasing with time, except for pixels with motion less than 5 m. This means that there is a minimum movement magnitude required to be able to predict a time-of-failure. This is also in agreement with the always increasing values of M_{pdf} for pixels of total motion less than 5 m. For other groups of pixels, P_3 is increasing with time to reach the highest values close to the rupture time. The probability P_3 for motions larger than 7 m surpass 0.7 in the 3 days before the real rupture time. P_3 is also much lower for larger motions before the 10th of June. This means that the number of false alarms is considerably reduced by selecting only pixels with larger motions. We can evaluate the quality of the prediction by comparing P_3 in the first weeks of the acceleration and in the days just before the failure. For pixels of motion magnitudes greater than 7 m, P_3 ranges from 0.15 to 0.8, showing the ability of this predictor to evaluate the proximity of the landslide to the rupture.

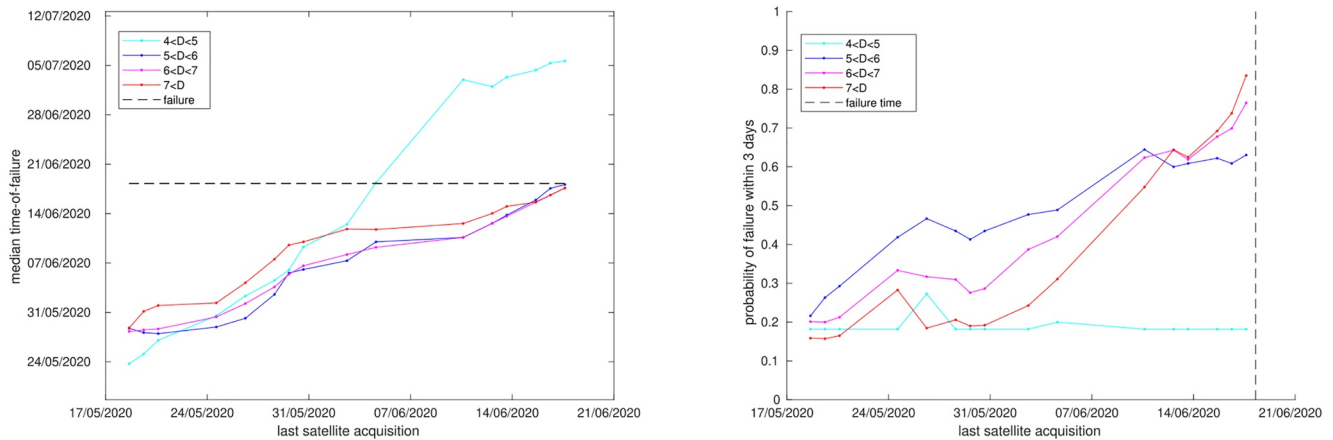


Figure 4. Time-of-failure median prediction (a) and probability to have a failure within 3 days (b) as a function of the last satellite image acquisition and for different motion magnitudes.

4. Discussion

4.1. Pre-Failure Acceleration

The satellite observations processed here, provide clear evidence that the landslide final stage of acceleration was not initiated during the dry season, but started at least in March during the rainy period. It must be noted that the 2020 rainy season was the rainiest season for at least 20 years, with clear impacts on the landslides of the area. For instance, on the nearby slow-moving Maca landslide situated in the same geology (lacustrine sediments), the displacement reaches 10 m in 2020, more than the 7 m of the very active year 2012 (Zerathe et al., 2016). For that reason, and also due to its similarity with the Maca landslide, we can suspect the rain infiltration and/or the river erosion to be serious controlling factors of the Achoma landslide. Ground water storage might possibly play a role in the delayed acceleration of the landslide, as it is observed on many different slow-moving landslides (e.g., Bièvre et al., 2018) and in particular on the nearby Maca landslide (Zerathe et al., 2016). However in Maca, despite the motion continues for weeks after the rainy season, the velocity decreases with time. Here we observe the opposite behavior, with an acceleration toward the failure, discarding the ground water storage as the final landslide trigger. An analysis of the seismicity, obtained by a local seismic network operated by the IGP (Instituto Geofísico del Perú) with completeness magnitude of M_l 3.5 doesn't show earthquakes greater than 4 in the vicinity of the landslide in the first 7 months of 2020. During that period, the largest earthquake recorded in the 50 km from the landslide was M_l 3.9, and the closest earthquake was 10 km away from the landslide (Figure S12 in Supporting Information S1). Therefore, it is highly improbable that an earthquake produced this acceleration (Bontemps et al., 2020).

The pattern of progressive acceleration observed here follows a Voights law (Voight, 1989), typical of the last stage of tertiary creep, showing that the landslide failure is certainly linked to a process of progressive damage and fault maturation. This observation reinforces the hypothesis of a long process of landslide triggering, where the landslide acceleration is only the final stage of damage localization along a shear band (Zvelebill & Moser, 2001). The α coefficient of the Voight's law is spatially homogeneous (Figure S7 in Supporting Information S1), showing that the deformation occurs at depth, without much fracturation inside the moving mass. The variability of the motion magnitude is mainly caused by the rotational aspect of the failure surface that will change the ratio between the vertical and the horizontal motions. The exponent of the Voight's law is 2.14 ± 0.12 , in the upper range of what is usually observed on other landslides (Intrieri et al., 2019). This high exponent may explain the long time-period of landslide acceleration. Indeed 3 months of landslide progressive pre-failure acceleration is in the upper limit of what is usually observed for this last stage of acceleration on other landslides (Federico et al., 2012; Scoppettuolo et al., 2020). Usually this phase can last between a few minutes to about 100 days for different types of rocks/soils and mechanisms (rockfalls, slides, toppling, ...).

We can also wonder if ground movements were preceding this final acceleration, as landslide kinematics can fluctuate at different time-scales (seasonally, interannually) depending on the controlling factors of the landslide motion (e.g., seasonal rainfalls). On the Achoma landslide, the pattern of motion before March 2020 is not clear,

displaying a general trend, but the uncertainties of the process prevent the detection of fluctuations of the motion with time. InSAR processing would therefore be of interest to study the controlling factors of this landslide kinematics in the years before the final acceleration.

4.2. Time-Of-Failure Prediction

The process developed here allows us to predict the time-of-failure 3 weeks before the rupture with a precision of 8 days, for the points of largest motion magnitudes. The larger the motion magnitudes, the better the prediction. Using the probability of failure within 3 days, we show that the number of false alarms is highly reduced when selecting only the pixels of largest motion magnitudes, due to the large uncertainties of the displacement time-series from PlanetScope images. Despite the specific algorithm used to retrieve the velocities from the displacement time-series, the prediction is not possible for motions of magnitudes lower than 5 m, that is about six times the displacement field uncertainties obtained with PlanetScope. These encouraging results show the real advantage of the high frequency of PlanetScope image acquisition, which allows us to obtain a dense time-series of displacement, and therefore to improve the sampling of the pre-failure acceleration. This is important especially for the velocity estimate, which can be altered by the uncertainty of the displacement measurements from satellites.

A large number of predictions are providing a time-of-failure before the time of the last image acquisition, which is simply not possible. These false alarms are caused by the measurement uncertainties and by an α coefficient larger than 2 (mean of 2.14). For this reason the inverse velocity model should always bias the prediction toward lower time-of-failure. We partially solved this issue by adapting the linear fit of the inverse velocity model with time using a linear fit weighted by the inverse uncertainties of the velocities, thus providing more importance to the last (and fastest) measurements. To fully overcome this problem of α different than 2, other prediction methods should be tested. The method proposed by Hao et al. (2016), linear with α , seems appealing. However, this method requires the computation of not only the first but also the second derivative of the displacement time-series, which will be tricky to implement on the optical satellite measurements, due to their large uncertainties. Instead, we believe that further developments should try to find an analytical expression of the Fukuzono model in terms of displacement and not velocity.

Despite the relative success of this Achoma case-study for landslide prediction, we believe it is not representative of the majority of the landslides, and the time-of-failure prediction from space will be rather complex for the majority of other landslides. Indeed, first of all, the Achoma landslide was large enough to be easily detected and spatially covered by satellites, which enabled us to compute statistics. Then its location and time-of-failure, 2 months after the end of the rainy season, occurred in an area with little cloud cover, so that satellite acquisitions were cloud-free very often over the 2 last months before the failure. Finally its period of acceleration was fairly long (3 months), and rather slow acceleration as shown by the α coefficient greater than 2. These two factors enable a good sampling of the landslide acceleration period. For all these reasons, we believe Achoma was an “ideal” case-study for this time-of-failure prediction from optical satellite images. It is not obvious that existing SAR satellites can do better than optical for this purpose. Indeed, InSAR presents other challenges like phase unwrapping of small objects, with phase-ambiguities even more complex to fix with the recent loss in 2022 of the Sentinel-1B satellite. The future launch of the combined L- and S-bands NiSAR radar satellite, with 2–5 days revisit time and longer wavelength, will greatly improve the capabilities of SAR satellites for time-of-failure prediction.

Finally, the prediction from satellites, either SAR or optical, relies on time-series of ground deformation. This prediction has an interest mostly in cases where a time-series of ground displacement can be automatically generated and a slow-moving landslide automatically detected. In the case of PlanetScope images, the automatic generation of ground displacement suffers from the image selection process which is a manual step, involving selecting the images acquired with similar orientations and without cloud-cover. For landslide detection (and therefore prediction) from PlanetScope images, it would be worth working on the automatic selection of the images.

5. Summary and Conclusions

Based on a 2.5 years time-series of ground displacement obtained from PlanetScope optical satellites, we document new observations of a landslide accelerating toward the rupture with an unprecedented view of the time and

spatial variability of the landslide pre-failure acceleration, thanks to the high revisit time of the PlanetScope constellation. We show that the Achoma landslide situated in South Peru was preceded by a progressive acceleration lasting between 3 and 3.5 months, reaching 8.1 m of precursory motions before its failure. These new observations allow us to model the physics of this acceleration with a high spatial density, that follows a Fukuzono model with a spatially homogeneous parameter $\alpha = 2.14$. Using an adapted algorithm to calculate the time-series of landslide velocity, we show that the inverse-velocity model can be used to predict the landslide time-of-failure from satellite data. This prediction is improving and false alarms decreasing for the pixels of largest displacement, providing a less than 8 days precision within the last 3 weeks before the failure for pixels of the landslide with motion greater than 7 m, which is about 10 times the PlanetScope motion uncertainties.

Despite this relative success for landslide prediction, we believe this case-study would not be representative of the majority of landslides, and that the prediction from PlanetScope satellites for other landslides could be more tricky. Indeed the Achoma landslide is in the upper limit of the tertiary creep duration, and occurred during a time-period with 2 months of clear sky, allowing a very good time sampling of the landslide with satellite images. Furthermore the prediction seems reliable only for pixels with large displacements before failure (greater than 5 m), which is not so common. Other case studies should be analyzed to validate the ability of optical high frequency satellites to predict the time-of-failure of landslides. This case-study opens new opportunities to detect pre-rupture landslide acceleration, but also questions the ability of optical satellites to predict their time-of-failure.

Data Availability Statement

All the PlanetScope images are publicly available on the PlanetScope webserver (<https://www.planet.com/explorer/>) through a free registration that gives access to a certain quota of images, not limited for academic users. The mic-mac software is available at <https://micmac.engg.eu/index.php/Accueil>. The TIO module is available at <https://sourcesup.renater.fr/www/tio/>. The time-series of velocity maps, and the Pléiades and drone DEMs are openly available in the Zenodo repository associated to this work <https://zenodo.org/record/7866962>.

Acknowledgments

P.L. would like to thank the CNES for providing the Pléiades images. This study benefited from the support of the Coup-erin consortium for open science.

References

- Azimi, C., Biarez, J., Desvarreux, P., & Keime, F. (1988). Prédiction d'éboulement en terrain gypseux. In *International symposium on landslides* (Vol. 5, pp. 531–536).
- Bhandari, R. (1988). In *Some practical lessons in the investigation and field monitoring of landslides* (Vol. 3, pp. 1435–1457). Lausanne.
- Bièvre, G., Joseph, A., & Bertrand, C. (2018). *Preferential water infiltration path in a slow-moving clayey Earthslide evidenced by cross-correlation of hydrometeorological time series (charlaix landslide, French western Alps)*. Geofluids (Online).
- Bontemps, N., Lacroix, P., & Doin, M.-P. (2018). Inversion of deformation fields time-series from optical images, and application to the long term kinematics of slow-moving landslides in Peru. *Remote Sensing of Environment*, 210, 144–158. <https://doi.org/10.1016/j.rse.2018.02.023>
- Bontemps, N., Lacroix, P., Larose, E., Jara, J., & Taipe, E. (2020). Rain and small earthquakes maintain a slow-moving landslide in a persistent critical state. *Nature Communications*, 11(1), 1–10. <https://doi.org/10.1038/s41467-020-14445-3>
- Bozzano, F., Mazzanti, P., & Moretto, S. (2018). Discussion to: “Guidelines on the use of inverse velocity method as a tool for setting alarm thresholds and forecasting landslides and structure collapses” by T. Carlà, E. Intrieri, F. Di Traglia, T. Nolesini, G. Gigli and N. Casagli. *Landslides*, 15(7), 1437–1441. <https://doi.org/10.1007/s10346-018-0976-2>
- Bruckl, E., & Parotidis, M. (2001). Estimation of large-scale mechanical properties of a large landslide on the basis of seismic results. *International Journal of Rock Mechanics and Mining Sciences*, 38(6), 877–883. [https://doi.org/10.1016/S1365-1609\(01\)00053-3](https://doi.org/10.1016/S1365-1609(01)00053-3)
- Bruckl, E., & Parotidis, M. (2005). Prediction of slope instabilities due to deep-seated gravitational creep. *Natural Hazards and Earth System Sciences*, 5(2), 155–172. <https://doi.org/10.5194/nhess-5-155-2005>
- Carlà, T., Intrieri, E., Di Traglia, F., Nolesini, T., Gigli, G., & Casagli, N. (2017). Guidelines on the use of inverse velocity method as a tool for setting alarm thresholds and forecasting landslides and structure collapses. *Landslides*, 14(2), 517–534. <https://doi.org/10.1007/s10346-016-0731-5>
- Carlà, T., Intrieri, E., Raspini, F., Bardi, F., Farina, P., Ferretti, A., et al. (2019). Perspectives on the prediction of catastrophic slope failures from satellite InSAR. *Scientific Reports*, 9(1), 1–9. <https://doi.org/10.1038/s41598-019-50792-y>
- Casagli, N., Intrieri, E., Tofani, V., Gigli, G., & Raspini, F. (2023). Landslide detection, monitoring and prediction with remote-sensing techniques. *Nature Reviews Earth & Environment*, 4(1), 51–64. <https://doi.org/10.1038/s43017-022-00373-x>
- Crosta, G. B., & Agliardi, F. (2003). Failure forecast for large rock slides by surface displacement measurements. *Canadian Geotechnical Journal*, 19(1), 176–191. <https://doi.org/10.1139/T02-085>
- Eberhardt, E., Stead, D., & Coggan, J. (2004). Numerical analysis of initiation and progressive failure in natural rock slopes—The 1991 Randa rockslide. *International Journal of Rock Mechanics and Mining Sciences*, 41(1), 69–87. [https://doi.org/10.1016/S1365-1609\(03\)00076-5](https://doi.org/10.1016/S1365-1609(03)00076-5)
- Federico, A., Popescu, M., Elia, G., Fidelibus, C., Internò, G., & Murianni, A. (2012). Prediction of time to slope failure: A general framework. *Environmental Earth Sciences*, 66(1), 245–256. <https://doi.org/10.1007/s12665-011-1231-5>
- Forlati, F., Gioda, G., & Scavia, C. (2001). Finite element analysis of a deep-seated slope deformation. *Rock Mechanics and Rock Engineering*, 34(2), 135–159. <https://doi.org/10.1007/s006030170019>
- Fukuzono, T. (1985). A new method for predicting the failure time of a slope. In *Proceedings of 4th international conference and field workshop on landslide*, 1985 (pp. 145–150).
- Handwergler, A. L., Huang, M.-H., Fielding, E. J., Booth, A. M., & Bürgmann, R. (2019). A shift from drought to extreme rainfall drives a stable landslide to catastrophic failure. *Scientific Reports*, 9(1), 1–12. <https://doi.org/10.1038/s41598-018-38300-0>

- Handwerger, A. L., Roering, J. J., & Schmidt, D. A. (2013). Controls on the seasonal deformation of slow-moving landslides. *Earth and Planetary Science Letters*, 377, 239–247. <https://doi.org/10.1016/j.epsl.2013.06.047>
- Handwerger, A. L., Roering, J. J., Schmidt, D. A., & Rempel, A. W. (2015). Kinematics of earthflows in the northern California coast ranges using satellite interferometry. *Geomorphology*, 246, 321–333. <https://doi.org/10.1016/j.geomorph.2015.06.003>
- Hao, S., Liu, C., Lu, C., & Elsworth, D. (2016). A relation to predict the failure of materials and potential application to volcanic eruptions and landslides. *Scientific Reports*, 6(1), 27877. <https://doi.org/10.1038/srep27877>
- Höhle, J., & Höhle, M. (2009). Accuracy assessment of digital elevation models by means of robust statistical methods. *ISPRS Journal of Photogrammetry and Remote Sensing*, 64(4), 398–406. <https://doi.org/10.1016/j.isprsjprs.2009.02.003>
- Intrieri, E., Carlà, T., & Gigli, G. (2019). Forecasting the time of failure of landslides at slope-scale: A literature review. *Earth-Science Reviews*, 193, 333–349. <https://doi.org/10.1016/j.earscirev.2019.03.019>
- Intrieri, E., Raspini, F., Fumagalli, A., Lu, P., Del Conte, S., Farina, P., et al. (2018). The Maoxian landslide as seen from space: Detecting precursors of failure with sentinel-1 data. *Landslides*, 15(1), 123–133. <https://doi.org/10.1007/s10346-017-0915-7>
- Iverson, R. M., & Major, J. J. (1987). Rainfall, ground-water flow, and seasonal movement at Minor Creek landslide, northwestern California: Physical interpretation of empirical relations. *Geological Society of America Bulletin*, 99(4), 579–594. [https://doi.org/10.1130/0016-7606\(1987\)99<579:RGFASM>2.0.CO;2](https://doi.org/10.1130/0016-7606(1987)99<579:RGFASM>2.0.CO;2)
- Lacroix, P., Araujo, G., Hollingsworth, J., & Taïpe, E. (2019). Self-entrainment motion of a slow-moving landslide inferred from landsat-8 time series. *Journal of Geophysical Research: Earth Surface*, 124(5), 1201–1216. <https://doi.org/10.1029/2018j004920>
- Lacroix, P., Berthier, E., & Maquerhua, E. T. (2015). Earthquake-driven acceleration of slow-moving landslides in the Colca valley, Peru, detected from Pléiades images. *Remote Sensing of Environment*, 165, 148–158. <https://doi.org/10.1016/j.rse.2015.05.010>
- Lacroix, P., Bièvre, G., Pathier, E., Kniess, U., & Jongmans, D. (2018). Use of sentinel-2 images for the detection of precursory motions before landslide failures. *Remote Sensing of Environment*, 215, 507–516. <https://doi.org/10.1016/j.rse.2018.03.042>
- Lacroix, P., Dehecq, A., & Taïpe, E. (2020). Irrigation-triggered landslides in a Peruvian desert caused by modern intensive farming. *Nature Geoscience*, 13(1), 56–60. <https://doi.org/10.1038/s41561-019-0500-x>
- Li, M., Zhang, L., Ding, C., Li, W., Luo, H., Liao, M., & Xu, Q. (2020). Retrieval of historical surface displacements of the baige landslide from time-series SAR observations for retrospective analysis of the collapse event. *Remote Sensing of Environment*, 240, 111695. <https://doi.org/10.1016/j.rse.2020.111695>
- Moretto, S., Bozzano, F., Esposito, C., Mazzanti, P., & Rocca, A. (2017). Assessment of landslide pre-failure monitoring and forecasting using satellite SAR interferometry. *Geosciences*, 7(2), 36. <https://doi.org/10.3390/geosciences7020036>
- Mufundirwa, A., Fujii, Y., & Kodama, J. (2010). A new practical method for prediction of geomechanical failure-time. *International Journal of Rock Mechanics and Mining Sciences*, 47(7), 1079–1090. <https://doi.org/10.1016/j.ijrmms.2010.07.001>
- Muller, J. R., & Martel, S. J. (2000). Numerical models of translational landslide rupture surface growth. *Pure and Applied Geophysics*, 157(6–8), 1009–1038. <https://doi.org/10.1007/s000240050015>
- Pham, M. Q., Lacroix, P., & Doin, M. P. (2018). Sparsity optimization method for slow-moving landslides detection in satellite image time-series. *IEEE Transactions on Geoscience and Remote Sensing*, 57(4), 2133–2144. <https://doi.org/10.1109/tgrs.2018.2871550>
- Poli, P. (2017). Creep and slip: Seismic precursors to the nuugaatsiaq landslide (Greenland). *Geophysical Research Letters*, 44(17), 8832–8836. <https://doi.org/10.1002/2017gl075039>
- Provost, F., Michéa, D., Malet, J.-P., Boissier, E., Poinat, E., Stumpf, A., et al. (2022). Terrain deformation measurements from optical satellite imagery: The MPIC-OPT processing services for geohazards monitoring. *Remote Sensing of Environment*, 274, 112949. <https://doi.org/10.1016/j.rse.2022.112949>
- Rose, N. D., & Hungr, O. (2007). Forecasting potential rock slope failure in open pit mines using the inverse-velocity method. *International Journal of Rock Mechanics and Mining Sciences*, 44(2), 308–320. <https://doi.org/10.1016/j.ijrmms.2006.07.014>
- Roy, D. P., Huang, H., Houborg, R., & Martins, V. S. (2021). A global analysis of the temporal availability of planetscope high spatial resolution multi-spectral imagery. *Remote Sensing of Environment*, 264, 112586. <https://doi.org/10.1016/j.rse.2021.112586>
- Rupnik, E., Daakir, M., & Deseilligny, M. P. (2017). Micmac—a free, open-source solution for photogrammetry. *Open Geospatial Data, Software and Standards*, 2(1), 1–9.
- Saito, M. (1969). Forecasting time of slope failure by tertiary creep. In *Proceedings of the 7th international conference on soil mechanics and foundation engineering, Mexico City, Mexico* (Vol. 2, pp. 677–683).
- Schöpa, A., Chao, W.-A., Lipovsky, B. P., Hovius, N., White, R. S., Green, R. G., & Turowski, J. M. (2018). Dynamics of the Askja caldera July 2014 landslide, Iceland, from seismic signal analysis: Precursor, motion and aftermath. *Earth Surface Dynamics*, 6(2), 467–485. <https://doi.org/10.5194/esurf-6-467-2018>
- Scoppettuolo, M., Cascini, L., & Babilio, E. (2020). Typical displacement behaviours of slope movements. *Landslides*, 17(5), 1105–1116. <https://doi.org/10.1007/s10346-019-01327-z>
- Sharifi, S., Hendry, M. T., Macciotta, R., & Evans, T. (2022). Evaluation of filtering methods for use on high-frequency measurements of landslide displacements. *Natural Hazards and Earth System Sciences*, 22(2), 411–430. <https://doi.org/10.5194/nhess-22-411-2022>
- Vela Valdez, J. C., & Chacaltana, C. A. (2020). *Deslizamiento de achoma ocurrido el 18 de junio del 2020* (Tech. Rep. No. A7066). INGEMMET.
- Voight, B. (1989). A relation to describe rate-dependent material failure. *Science*, 243(4888), 200–203. <https://doi.org/10.1126/science.243.4888.200>
- Zerathe, S., Lacroix, P., Jongmans, D., Marino, J., Taïpe, E., Wathélet, M., et al. (2016). Morphology, structure and kinematics of a rainfall controlled slow-moving Andean landslide, Peru: The Maca slow-moving Andean landslide. *Earth Surface Processes and Landforms*, 41(11), 1477–1493. <https://doi.org/10.1002/esp.3913>
- Zhang, Y.-G., Tang, J., He, Z.-Y., Tan, J., & Li, C. (2021). A novel displacement prediction method using gated recurrent unit model with time series analysis in the Erdaohe landslide. *Natural Hazards*, 105(1), 783–813. <https://doi.org/10.1007/s11069-020-04337-6>
- Zvelebil, J., & Moser, M. (2001). Monitoring based time-prediction of rock falls: Three case-histories. *Physics and Chemistry of the Earth - Part B: Hydrology, Oceans and Atmosphere*, 26(2), 159–167. [https://doi.org/10.1016/S1464-1909\(00\)00234-3](https://doi.org/10.1016/S1464-1909(00)00234-3)

References From the Supporting Information

- Berthier, E., Arnaud, Y., Kumar, R., Ahmad, S., Wagnon, P., & Chevallier, P. (2007). Remote sensing estimates of glacier mass balances in the Himachal Pradesh (Western Himalaya, India). *Remote Sensing of Environment*, 108(3), 327–338. <https://doi.org/10.1016/j.rse.2006.11.017>
- Lacroix, P. (2016). Landslides triggered by the Gorkha earthquake in the Langtang valley, volumes and initiation processes. *Earth Planets and Space*, 68(1), 46. <https://doi.org/10.1186/s40623-016-0423-3>
- Shean, D. E., Alexandrov, O., Moratto, Z. M., Smith, B. E., Joughin, I. R., Porter, C., & Morin, P. (2016). An automated, open-source pipeline for mass production of digital elevation models (DEMs) from very-high-resolution commercial stereo satellite imagery. *ISPRS Journal of Photogrammetry and Remote Sensing*, 116, 101–117. <https://doi.org/10.1016/j.isprsjprs.2016.03.012>

Erratum

The originally published version of this article incorrectly gave the name of the third coauthor, L. Albinez, as “L. A. Angel.” This error appeared in the main author list, the citation, the author contributions, and Supporting Information S1. The error has been corrected, and this may be considered the authoritative version of record.